Analytical Methods

ROYAL SOCIETY OF CHEMISTRY

PAPER

View Article Online
View Journal | View Issue

Cite this: *Anal. Methods*, 2026, **18**, 1270

Integrated LIBS-Raman spectroscopic platform for concurrent elemental and molecular analysis

Sungho Shin, [a] John Park [b] and Duk-Jo Kong *[ab]

Microplastic particles (MPs) are emerging environmental contaminants that can adsorb toxic metals and organic species, posing risks to ecosystems and human health. In this study, a compact analytical platform combining laser-induced breakdown spectroscopy (LIBS) and Raman spectroscopy (RS) was developed for the simultaneous molecular and elemental analysis of polymer microbeads. The system shares a common optical path for consecutive acquisition of LIBS and Raman signals from the same spot, enabling direct correlation between polymer identity and adsorbed metal content. Characteristic Raman bands successfully discriminated polystyrene (PS), polyethylene (PE), and polypropylene (PP), while LIBS analysis of metal-exposed PS beads revealed distinct Pb I (405.8 nm) and Cu I (324.8 nm) lines with concentration-dependent intensities. Quantitative calibration yielded limits of detection of 2.29 ppm for Pb and 1.61 ppm for Cu, based on the Pb I 405.8 nm and Cu I 324.8 nm lines, respectively. Machine learning-based clustering of Raman spectra, including Gaussian mixture model and k-means approaches, achieved up to 99.3% unsupervised classification accuracy. The results demonstrate that the integrated LIBS-RS system provides analytical performance comparable to laboratory-scale LIBS instruments, while offering the added capability of molecular fingerprinting for field-deployable microplastic and contaminant monitoring.

Received 28th October 2025
Accepted 8th January 2026

DOI: 10.1039/d5ay01789k

rsc.li/methods

Introduction

Microplastic particles (MPs), typically defined as plastic debris smaller than 5 mm, have become ubiquitous environmental contaminants originating from degradation of larger plastic waste, textile fibers, and industrial abrasives.[1,2] Continuous discharge from wastewater effluents, tire wear, and domestic washing contributes to the accumulation of MPs in aquatic environments, including surface waters and drinking-water systems.[3] Recent investigations have revealed that MPs can be detected even in tap water and bottled water samples, suggesting a direct route of human exposure through ingestion and inhalation.[4] Once internalized, MPs have been reported to penetrate biological barriers, accumulate in tissues such as the liver and lungs, and induce oxidative stress and inflammatory responses, raising concerns about their potential toxicity to humans.

Beyond their physical presence, MPs can act as vectors for hazardous substances. Hydrophobic polymer surfaces readily adsorb persistent organic pollutants, pathogenic microorganisms, and particularly heavy metals such as Pb, Cu, Cd, and Zn.[5,6] These metals can accumulate on MPs *via* complexation or electrostatic interactions and be transported across ecosystems, resulting in secondary pollution and enhanced bioavailability.[7] Therefore, analytical techniques that can simultaneously characterize both the polymer identity and the associated chemical species are urgently required.

Several instrumental approaches have been employed for MP characterization and contaminant analysis, including Fourier-transform infrared (FT-IR) microscopy, inductively coupled plasma-mass spectrometry (ICP-MS), and electron microscopy.[8,9] While FT-IR spectroscopy provides molecular information on polymer composition, they are typically limited to organic species and require long acquisition times and intensive data processing. ICP-MS or atomic absorption spectroscopy (AAS), in contrast, can quantify heavy metals with high sensitivity but require complete sample digestion and loss of spatial information. These conventional methods are thus time-consuming, destructive, and lack the ability to provide correlated chemical and elemental mapping at the single-particle level.

To overcome these drawbacks, laser-induced breakdown spectroscopy (LIBS) and Raman spectroscopy (RS) have emerged as complementary, rapid, and minimally destructive optical techniques. LIBS is based on plasma emission generated by a high-energy laser pulse on the sample surface, providing multi-elemental information across the periodic table without sample preparation.[10] RS, conversely, probes inelastic photon scattering induced by molecular vibrations, enabling

[a]*GIST InnoCORE Research Center, Gwangju Institute of Science and Technology, 61005 Gwangju, Republic of Korea*

[b]*Graduate School of AI Policy and Strategy, Gwangju Institute of Science and Technology, 61005 Gwangju, Republic of Korea. E-mail: dukjokong@gist.ac.kr*

fingerprint identification of polymer types and organic functional groups.[11] Since the two methods are governed by distinct physical processes including atomic emission in LIBS and molecular vibration in RS, their combination offers a powerful route for simultaneous detection of organic and inorganic constituents in complex samples and rapid and *in situ* elemental analysis at the single-particle level, while conventional analytical techniques such as ICP-MS and AAS provide superior sensitivity.[12,13]

Recent advances in LIBS and RS have focused on improving quantitative accuracy and lowering detection limits. Notably, picosecond laser and calibration-free (CF-LIBS) significantly improves analytical accuracy and reduce matrix effect, allowing sub-ppm or ppb-level detection.[14,15] Several studies have also pushed LIBS detection limits to the ppb levels.[16,17] Similarly, surface-enhanced Raman spectroscopy (SERS) have emerged as a highly sensitive technique through the plasmon-mediated amplification.[18] Despite these advantages, such advanced configurations typically require complex optical setups, high-cost laser sources, and additional surface treatment, which limit their practicality for compact or field-deployable systems.

Several studies have demonstrated the utility of LIBS for detecting heavy-metal adsorption on polymeric or sediment matrices. For instance, N. Fayek *et al.* demonstrated the application of LIBS for heavy metal detection in complex organic matrices, which are challenges with polymer analysis.[19,20] Also, W. A. Farooq *et al.* analyzed several trace elements (Al, Si, P, Ca *etc.*) and molecular lines (Cn, CO, C_2 and CH) in polymer materials.[21] In parallel, RS has been widely utilized for classification of various polymer types in environmental and laboratory-aged samples.[22] These prior efforts confirm that both LIBS and RS can independently provide key compositional information but still require separate instruments and measurement steps. Recent research has sought to integrate LIBS and RS into a single optical platform, leveraging shared optics and synchronized laser operation to enable simultaneous molecular and elemental analysis.[23,24] Integrating both techniques minimizes alignment errors between measurement spots and allows rapid correlation between the chemical identity of polymers and the elemental composition of adsorbed contaminants.

In this work, we evaluated a combined LIBS and RS system for the analysis of MPs and heavy-metal contamination. The proposed platform enables both spectral modalities to share a common optical path, allowing consecutive acquisition of emission and scattering spectra from the same target area. Using three types of certified plastic beads as model MPs, and Pb/Cu solutions as representative metal contaminants, we demonstrate that the proposed system can discriminate polymer types and quantify metal adsorption *via* calibration-based LIBS analysis. The 3-sigma criterion limit of detection (LOD) for Pb and Cu was evaluated to assess quantitative feasibility. The present study adopts a nanosecond-based combined LIBS-Raman platform as a deliberate compromise between analytical performance and system practicality. Rather than targeting ultimate sensitivity achievable with ultrafast or calibration-free approaches, the proposed system emphasizes robust low-ppm quantification, compatibility with semi-portable instrumentation, and molecular–elemental correlation, thereby addressing key requirements for microplastic and environmental contamination monitoring.

Experimental

Materials

Three types of plastic beads were prepared for combined LIBS and RS measurements: polypropylene (PP; 428116; Sigma-Aldrich), polyethylene (PE; 428043; Sigma-Aldrich), and polystyrene (PS; 441147; Sigma-Aldrich). The average diameters of the beads were approximately 3.5 mm, 3.0 mm, and 2.5 mm, respectively. For spectral acquisition, each bead was mounted on a glass slide using an adhesive tape (3M), ensuring that the relatively flat top surface of the bead was oriented toward the incident laser beam.

To simulate heavy metal exposure, copper (Cu; 38996; Sigma-Aldrich) and lead (Pb; 16595; Sigma-Aldrich) standard solutions (1000 ppm stock solutions) were used. Working solutions with concentrations of 1, 10, 50, 100, and 1000 ppm were prepared by appropriate dilution with 2% nitric acid. For sample preparation, 25 mL of solution was used for concentrations ≤10 ppm, while 5 mL was used for concentrations >10 ppm. Five PS beads were immersed in each solution and exposed for five days. During the exposure period, continuous mixing was achieved using a centrifuge operated at 300 rpm to ensure homogeneous contact between the beads and the solutions as shown in Fig. 1.

Instruments

Fig. 1 illustrates the schematic configuration of the combined LIBS and RS system. All optical components and instruments were mounted on an optical board, with the three-axis translation stage (XYZ) positioned externally. The lasers, mirrors, and lenses were firmly fixed and aligned using a cage system.

For RS measurements, a continuous-wave laser (L1; CP532; Thorlabs) with a wavelength of 532 nm was employed. For LIBS measurements, a pulsed laser (L2; MicroJewel; Quantum Composers) operating at 1064 nm with a 6 ns pulse width was used. The shot-to-shot energy deviation of both lasers was

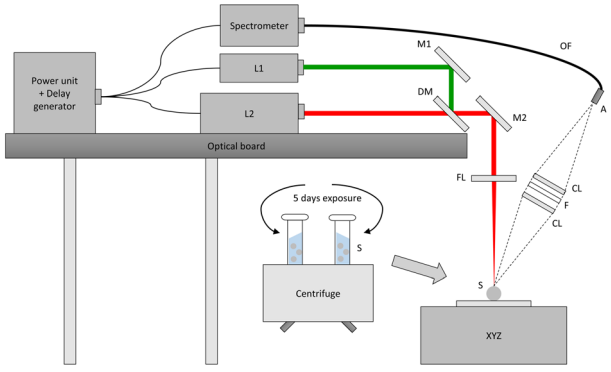

Fig. 1 Schematic of the sample preparation process and the combined LIBS and RS system.

experimentally evaluated and found to be less than 1.5%, indicating stable laser output during the measurements. To ensure collinearity of the two laser beams, a second-harmonic laser mirror (M1; NB1-K12; Thorlabs), a long-pass dichroic mirror (DM; DMLP650; Thorlabs), and a dual-order laser mirror (M2; NB1-K13; Thorlabs) were installed at 45° incidence. Both beams were then focused onto the sample surface through a lens with a 50 mm focal length (FL; AC254-050-AB-ML; Thorlabs). After focusing, the measured laser power and pulse energy were 5 mW and 10 mJ, respectively. The calculated beam spot sizes, defined as the $1/e^2$ beam diameters, were approximately 10 μm for the CW laser and 50 μm for the pulsed laser. These values were estimated using a Gaussian beam focusing model, based on the laser wavelength, focal length of the focusing lens, and the input beam diameter.[25]

Optical signals generated from LIBS emission and Raman scattering were collected at 45° relative to the sample surface (S). The collection optics consisted of two collection lenses (CL; LA4148-ML), a notch filter (F; NF533-17; Thorlabs), and an optical fiber adapter (A; SM05SMA; Thorlabs). The signals were guided by a 1 m optical fiber (OF; FC-UV1000-1; Avantes) into a compact CCD spectrometer (Avaspec-mini 2048CL OEM; Avantes) with a spectral range of 350–600 nm (1200 lines/mm grating), and a resolution of ~0.15 nm. The selected commercial CCD spectrometer of dimensions and weight are 95 × 68 × 20 mm^3 and 175 g, respectively. For LIBS acquisition, the gate delay and width were adjusted to 1 μs and 1.05 ms, respectively. Notably, the gate width corresponds to the minimum integration window supported by the compact CCD spectrometer used in this study. The gate delay was experimentally optimized during system development to maximize the signal-to-noise ratio by suppressing early-stage continuum emission under the fixed minimum gate width. Raman spectra were recorded with an exposure time of 0.5 second.

The entire system, including two lasers, beam-combining optics, and collection optics, was mounted on a single optical board with approximate dimensions of 20 × 15 × 7 cm^3. While the current implementation is not fully handheld, this footprint represents a semi-portable configuration that can be transported and deployed as a single integrated unit. A photograph of the assembled system is provided for reference only in the SI as shown in Fig. S1.

Data acquisition

Three types of plastic beads (PP, PE, and PS) were examined during RS signal measurements. Five beads were selected from each type, and ten laser irradiation spots were designated per bead. At each spot, ten Raman spectra were collected, resulting in a total of 500 spectra per plastic type (5 beads × 10 spots × 10 spectra). The spot positions were controlled using the XYZ translation stage, with a spacing of around 2 mm between adjacent spots. For bead samples, the laser was directed toward the central region of each bead to minimize edge effects.

To estimate the LOD of heavy metal exposures, ten distinct spots were examined on each bead, with a single laser shot per spot. Since five PS beads were used for each concentration condition, a total of 50 LIBS spectra were obtained per concentration. Including the control group, 300 LIBS spectra were collected in total and used to construct calibration curves for each target element. The integrated peak intensity was calculated as the area under the emission peak, excluding contributions from background regions.[26] The LOD was calculated according to the 3-sigma criterion, $3\sigma/s$, where s is the slope of the calibration curve and $\sigma$is the standard deviation of the blank (0 ppm) measurements.[27,28] Calibration curves were fitted using Origin (OriginLab) program.

Spectral processing and analysis

All spectroscopic data acquired from LIBS and RS were subjected to a standardized pre-processing procedure prior to both spectral and classification analysis. For both LIBS and RS measurements, the raw spectra were normalized by dividing the intensity at each wavelength by the integrated area of the entire spectrum. This total-area normalization effectively minimizes variations in absolute intensity caused by instrumental fluctuations or sampling geometry while preserving the relative distribution of spectral features.[29] In the case of Raman spectra, an additional smoothing step was applied using the Savitzky–Golay filter (polynomial order = 3, window size = 7), which has been widely reported as an effective method to reduce random noise while maintaining peak fidelity.[30] Following normalization and smoothing, averaged spectra were generated for both LIBS and Raman data, which were subsequently utilized for peak assignment and feature interpretation.

For classification of the plastic bead samples, unsupervised learning approaches were employed to evaluate the intrinsic separability of the data. To reduce the dimensionality of the high-resolution spectral data, principal component analysis (PCA) was performed.[31] The first ten principal components were retained, cumulatively explaining more than 95% of the total spectral variance, and these components were used as input features for clustering. To differentiate the three polymer bead types, unsupervised clustering was performed using two conventional algorithms: k-means and Gaussian Mixture Model (GMM). The k-means algorithm partitions spectra into k groups by minimizing the within-cluster variance between spectral vectors and their corresponding centroids.[32,33] The GMM algorithm models each cluster as a Gaussian probability distribution and estimates parameters through the Expectation-Maximization (EM) procedure, allowing for clusters with different shapes and covariances when compared with k-means methods.[34,35] Both algorithms were applied to the normalized Raman spectra without prior label information, providing a data-driven evaluation of spectral similarity and class separability among the three polymers.

To evaluate the quality of clustering results, the Adjusted Rand Index (ARI) was employed. ARI provides a normalized measure of similarity between predicted cluster labels and ground-truth class labels, adjusted for random chance.[36] Hungarian matching was further applied to align clusters with the corresponding true classes prior to reporting classification accuracy.[37] For comparative purposes, two supervised learning

methods commonly used in chemometric classification were additionally implemented. Linear Discriminant Analysis (LDA) was applied, while Support Vector Machines (SVMs) were also constructed with a radial basis function (RBF) kernel.[38,39] Both supervised methods were validated by 10-fold cross-validation, and confusion matrices were derived to quantitatively assess predictive performance.

Results and discussion

Spectral analysis

Representative Raman spectra of the three polymer bead samples including polystyrene (PS), polyethylene (PE), and polypropylene (PP) are shown in Fig. 2. For each polymer type, ten Raman spectra were recorded at individual surface spots, accumulated to improve the signal-to-noise ratio, and averaged over 50 measurements per material. The averaged and normalized spectra clearly exhibit distinct sets of characteristic bands corresponding to the molecular vibrations of each polymer, as summarized in Table 1.

The PS spectrum (black trace) is dominated by sharp and well-defined peaks at 992, 1156, and 1584 cm^{-1}, assigned to the ring-breathing and C–C stretching vibrations of the aromatic phenyl group.[40] Especially, the pronounced intensity near 1000 cm^{-1} arises from the symmetric ring-breathing vibration of the phenyl group. The PE spectrum (red trace) exhibits broad bands centered at 1050, 1120, 1289, and 1428 cm^{-1}, which are attributed to C–C stretching and CH_2 twisting/bending vibrations characteristic of aliphatic chains.[41] These bands indicate the presence of highly ordered crystalline domains typical of linear polyethylene structures. The PP spectrum (blue trace) reveals characteristic peaks at 825, 1140, 1314, and 1444 cm^{-1}. Each peak corresponds to CH_3 rocking and asymmetric bending of CH_3, consistent with previously reported Raman assignments for polypropylene.[42] Compared with PE, PP shows additional CH_3-related modes owing to the presence of side methyl groups on the polymer chain.

Table 1 Peak position and assignment of vibrational mode in polymer bead samples[40–42]

Peak position	Vibrational mode	Assignment
992 cm^{-1}	Ring breathing	PS
1156 cm^{-1}	C–C stretch	PS
1584 cm^{-1}	C═C stretch	PS
1050 cm^{-1}	C–C stretch	PE
1120 cm^{-1}	C–C stretch	PE
1289 cm^{-1}	CH_2 twist	PE
1428 cm^{-1}	CH_2 bend	PE
825 cm^{-1}	C–C stretch	PP
1140 cm^{-1}	C–C stretch	PP
1314 cm^{-1}	CH_3 bend	PP
1444 cm^{-1}	CH_2 bend	PP

The observed Raman patterns confirm that even under short-integration, moderate-power excitation, the three polymer types can be unambiguously identified by their diagnostic vibrational modes. For practical microplastic monitoring, these diagnostic bands can serve as reference markers for rapid spectral library matching in microplastic monitoring. Specifically, the C═C stretch of PS (~1584 cm^{-1}), the CH_2 twist of PE (~1289 cm^{-1}), and the C–C stretch and CH_3 rocking of PP (~825 cm^{-1}) can be used for material discrimination in mixed samples. Furthermore, the relatively high signal-to-noise ratios obtained from the accumulated spectra demonstrate the system's capability for low-power, non-destructive analysis, which is an essential requirement for portable field applications.

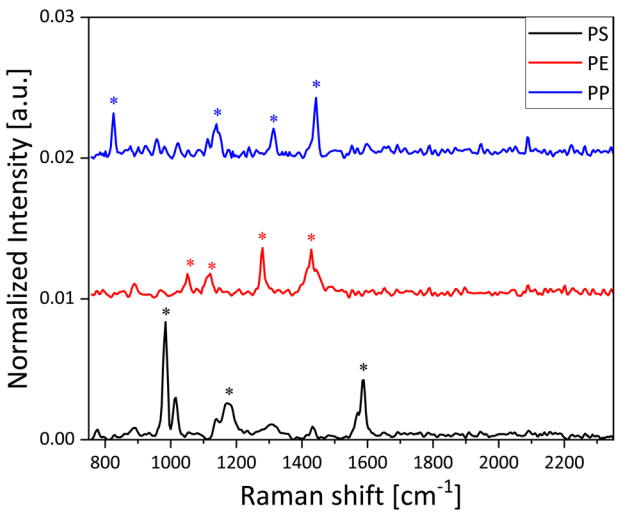

Fig. 2 Averaged spectra of PS (black line), PE (red line) and PP (blue line) beads using an excitation wavelength of 532 nm (RS measurement). Note that assignments of RS signal are marked as a symbol of *, representing in Table 1.

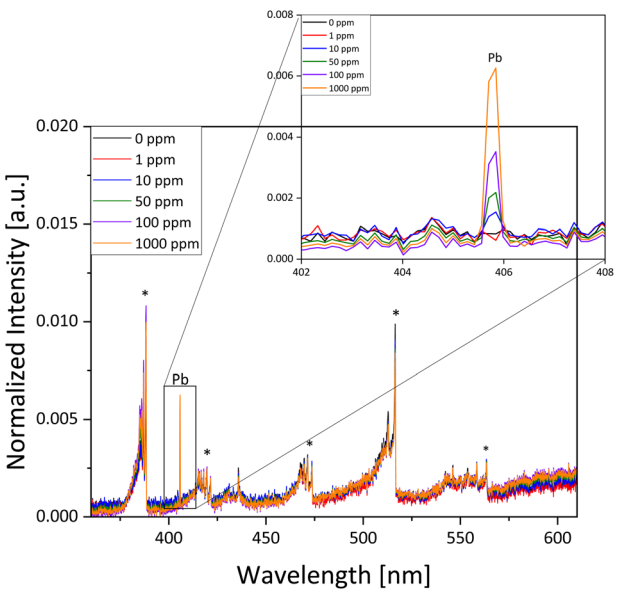

Fig. 3 Averaged spectra of PS bead, exposed in the concentrated Pb solution from 1 to 1000 ppm, using an irradiation wavelength of 1064 nm (LIBS measurement). Note that assignments of emission lines and molecular bands are marked as a symbol of *, as detailed in Tables 2 and 3, respectively.

Fig. 3 presents the averaged and normalized LIBS spectra of PS beads exposed to Pb solutions with concentrations ranging from 1 to 1000 ppm. Each spectrum was obtained by averaging 50 individual laser shots acquired from 10 distinct surface spots, followed by total-intensity normalization to compensate for shot-to-shot fluctuation. Prominent molecular bands are indicated by a symbol (*), with their respective assignments summarized in Table 2. The broadband features correspond to molecular CN and C_2 Swan bands that are commonly observed during LIBS analysis of polymeric or carbon-rich materials.[43] These bands arise from plasma recombination reactions of ablated carbon and nitrogen species from the polymer matrix. As shown in Table 2, the CN violet and C_2 Swan systems contribute to the main background structure but remain nearly constant in relative intensity across all Pb concentrations. For example, an averaged relative standard deviation (RSD) of CN violet ($\Delta v = -1$) area (from 410–420 nm range) was estimated at 5.03%. Their stability indicates that the plasma formation and ablation efficiency are consistent under identical irradiation conditions.

In contrast, the neutral atomic Pb I line at 405.8 nm, identified using the NIST Atomic Spectra Database, exhibits a clear and monotonic increase in intensity with rising Pb concentration (inset of Fig. 3). This trend demonstrates successful quantitative detection of Pb adsorbed onto the PS surface. For Cu analysis, emission peaks of Cu typically appear near 510–515 nm. However, this region overlaps strongly with the C_2 Swan band at 516.3 nm in the present spectra as shown in Fig. 3, complicating quantitative isolation of the Cu signal. To circumvent this spectral interference, a secondary spectrometer covering the 320–340 nm region was employed, where the Cu I line at 324.8 nm and 327.4 nm listed in Table 3 are free from molecular background. The resulting Cu emission profiles across all concentrations are provided in the SI as shown in Fig. S2.

Overall, the LIBS measurements clearly distinguished Pb and Cu emission lines from the persistent polymer-derived molecular bands. The observation that molecular bands remained invariant while Pb intensity increased with concentration supports the robustness of normalization and the quantitative potential of the combined LIBS-RS platform for trace-metal analysis on polymeric microbeads.

Multivariate analysis

To evaluate the classification performance of different machine learning approaches applied to Raman spectra of PP, PE, and PS polymer beads, both unsupervised and supervised algorithms were employed. The corresponding confusion matrices are shown in Fig. 4, and the two-dimensional t-SNE projections used for visual interpretation of clustering structures are presented in Fig. 5.

In the unsupervised framework, Gaussian Mixture Model (GMM) and k-means clustering were implemented to automatically group Raman spectral features without prior label information. To evaluate their clustering accuracy relative to the ground-truth labels, the predicted clusters were aligned using Hungarian matching, and quantitative performance was assessed *via* the Adjusted Rand Index (ARI). The resulting confusion matrices in Fig. 4(a) and (b) reflect these matched cluster–class correspondences. The GMM achieved an overall classification accuracy of 99.3%, slightly outperforming the k-means result (97.3%). This superior performance of the GMM can be attributed to its probabilistic modeling of class boundaries, which enables flexible representation of clusters with anisotropic covariance structures, in contrast to the rigid, spherical partitions assumed by k-means.[46]

The unsupervised methods include (a) Gaussian Mixture Model (GMM) and (b) k-means clustering, while the supervised methods correspond to (c) Linear Discriminant Analysis (LDA) and (d) Support Vector Machine (SVM). The t-SNE maps in Fig. 5(a) and (b) further visualize these differences. The t-SNE algorithm, a widely used nonlinear dimensionality reduction method in spectroscopic data analysis, was applied for visualization.[47] Both methods yielded three clearly separated clusters corresponding to PP (black), PE (blue), and PS (red), yet GMM produced more compact and well-defined cluster boundaries

Table 2 Peak wavelength of molecular bands of the emission lines[43,44]

Molecular species	Wavelength (nm)
CN violet ($\Delta v = +1$)	388.3
CN violet ($\Delta v = -1$)	419.7
C_2 swan ($\Delta v = +1$)	471.5
C_2 swan ($\Delta v = 0$)	516.3
C_2 swan ($\Delta v = -1$)	563.3

Table 3 Peak wavelength of neutral atomic Pb and Cu emission lines[45]

Elements	Wavelength (nm)
Pb I	405.8
Cu I	324.8
Cu I	327.4

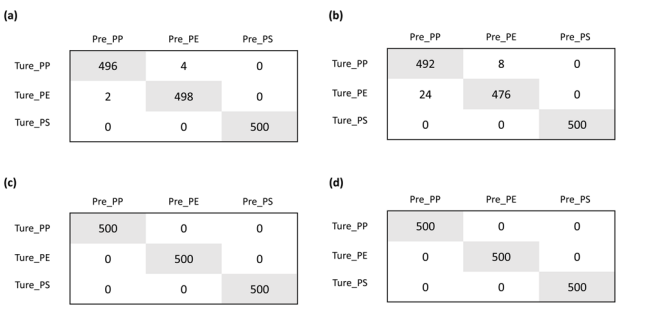

Fig. 4 Confusion matrices for the classification of Raman spectral datasets from PP, PE, and PS polymer beads. Panels (a) and (b) show the results for unsupervised clustering with GMM and k-means, respectively, with cluster labels matched to true classes *via* Hungarian matching. Panels (c) and (d) show the 10-fold cross-validation results for the supervised classifiers LDA and SVM.

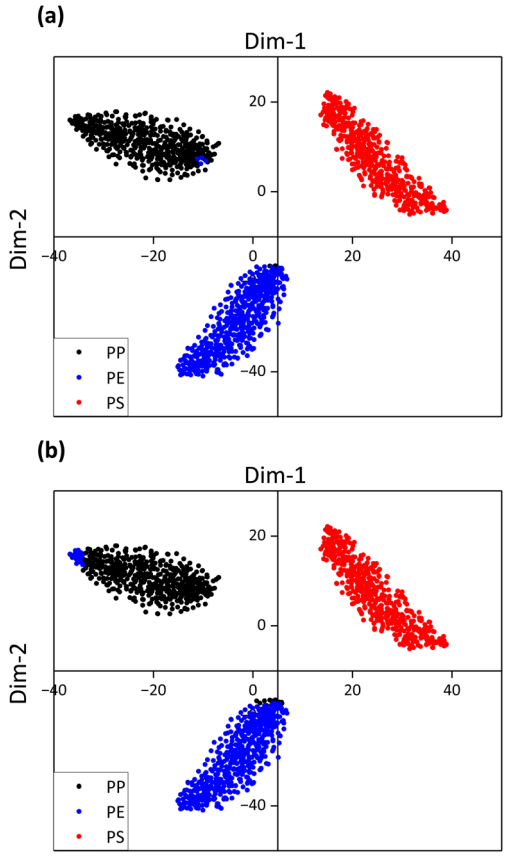

Fig. 5 2D t-SNE mapping of Raman spectral data for plastic bead classification: (a) GMM clusters; (b) k-means clusters for PP (black color), PE (blue color), and PS (red color) beads.

with minimal overlap, especially between PP and PE distributions. The k-means clusters showed slightly elongated shapes, reflecting its sensitivity to variance differences among spectral dimensions.

For comparison, supervised algorithms such as Linear Discriminant Analysis (LDA) and Support Vector Machine (SVM) were additionally performed using the same dataset with known class labels as shown in Fig. 4(c) and (d). Both methods achieved perfect classification (100% accuracy) across all polymer types, confirming that Raman spectral fingerprints are sufficiently distinct for linear separation in feature space. These results indicate that minimal model complexity is sufficient when Raman spectral bands exhibit strong class-specific intensity patterns.

In this study, the GMM yielded a slightly higher accuracy than k-means for an unsupervised classification of polymer-class Raman spectra. In polymer or microplastics spectroscopy, spectral variables are often correlated (shared vibrational envelopes) and class clouds show anisotropic covariance due to baseline, fluorescence, and band-ratio variability. Under these conditions, model-based clustering that learns full covariance (GMM) can better capture elliptical and partially overlapping manifolds than distance-based k-means.[35] Similar advantages of GMM have been documented in microplastics spectral screening workflows, where probabilistic mixtures improved cluster interpretability over hard partitions.[48] Moreover, B. Greve *et al.* reported that a method based on GMM seems to be more flexible compared with the commonly applied k-means method using a chemical data.

Collectively, the multivariate analysis confirms that both unsupervised and supervised learning methods can reliably classify polymer-specific Raman spectra, with GMM providing the most accurate unsupervised performance. These findings validate the suitability of machine-learning-assisted RS for automated identification of microplastic particles in complex mixtures.

Estimation of LOD

Fig. 6 presents the calibration curves derived from integrated emission intensities as a function of metal concentration for (a) Pb and (b) Cu, obtained from PS beads exposed to concentrations ranging from 1 to 1000 ppm. For each concentration, 50 LIBS spectra (10 spots × 5 beads) were averaged and normalized, and the resulting integrated peak intensities were plotted against concentration.

At higher concentrations, a clear deviation from linearity was observed, which is attributed to self-absorption and plasma saturation effects, particularly for resonance emission lines. Such behavior is well documented in LIBS analysis and typically

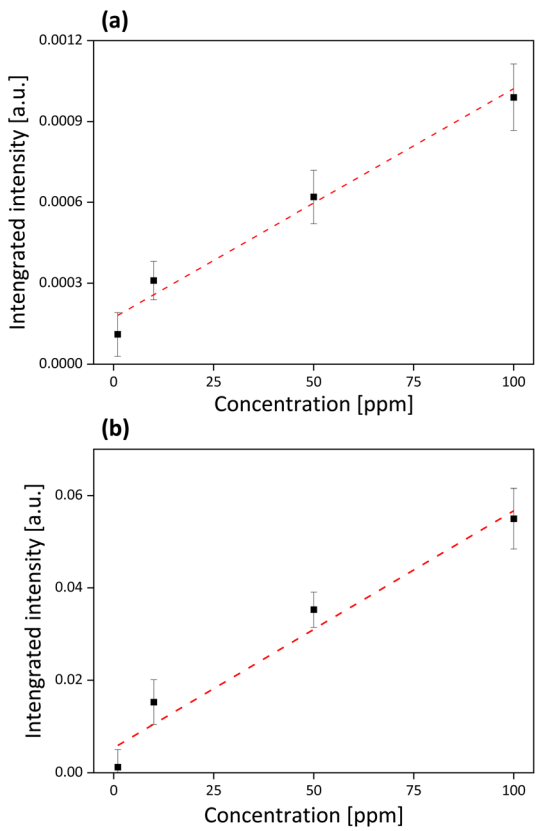

Fig. 6 Quantitative analysis of heavy metals using LIBS: calibration curves of (a) Pb; (b) Cu with linear fitting (red dashed lines).

limits the usable linear dynamic range for quantitative calibration. Self-absorption occurs when emitted photons are reabsorbed by atoms of the same species within the plasma, leading to nonlinear signal saturation.[49] This effect becomes more pronounced at elevated analyte concentrations and for strong resonance lines, such as the Cu I emission at 324.8 nm examined in this study.

Therefore, linear fitting (red dashed lines in Fig. 6) was intentionally restricted to the lower-concentration region (<100 ppm), where the relationship between integrated emission intensity and analyte concentration remained approximately linear and less affected by self-absorption. The limits of detection were calculated using the standard 3σ criterion, based on the slope of the linear calibration region and the standard deviation of the background signal. By excluding the non-linear high-concentration regime, the calculated LODs more accurately reflect the system's sensitivity for trace-level detection. Using this approach, the LODs were determined to be 2.29 ppm for Pb and 1.61 ppm for Cu, representing the practical analytical threshold of the semi-portable system for metal-loaded polymer beads under controlled measurement conditions.

The full calibration curves over the entire concentration range up to 1000 ppm, including the non-linear regime, are provided in the SI as shown in S3. These results confirm that beyond approximately 100 ppm, the Pb and Cu emission signals begin to saturate, consistent with self-absorption and matrix effects in polymer substrates.

In the context of previous literature, these LODs fall within a typical range for LIBS heavy-metal quantification on complex substrates. For example, Zhang *et al.* achieved LODs of around 1.5 ppm for Cr, Pb, and Cu in PMMA polymer matrices using a combined LIBS-machine learning approach.[50] Similarly, LIBS analysis of trace heavy metals in aqueous systems has reported detection limits in the range of ~1–5 ppm under single-pulse excitation conditions.[51] This agreement indicates that the semi-portable configuration adopted in the present work maintains a competitive analytical performance, while additionally providing molecular-level compositional information *via* Raman spectroscopy (RS). The dual-modality configuration therefore bridges the gap between elemental trace quantification and polymer identification within a single optical platform.

Several advanced quantitative strategies have been proposed to mitigate self-absorption effects in LIBS, including self-absorption correction (SAC) methods, internal standardization, and calibration-free approaches.[49,52,53] SAC techniques typically rely on plasma diagnostics, line-shape analysis, or the use of non-resonant emission lines to compensate for reabsorption losses. However, such correction schemes often require additional spectral lines, higher spectral resolution, which increases experimental and computational complexity.

In the present work, SAC-based corrections were not applied, as the primary objective was to evaluate the practical quantitative capability of a compact, nanosecond-based LIBS-Raman spectroscopic platform under simplified measurement conditions. Instead, quantitative rigor was ensured by restricting calibration to the low-concentration regime where self-absorption effects are minimal and well controlled. This strategy is consistent with established LIBS practices for trace-level analysis and is well suited for semi-portable systems intended for rapid environmental screening rather than high-concentration bulk quantification.

The portability and versatility of the present system highlight its potential for in-field environmental applications, particularly for real-time screening of metal-adsorbed microplastics in aquatic systems. By integrating LIBS and RS data, future work can enable automated classification of microplastic particles according to both polymer type and contamination level. Such integration would significantly enhance environmental monitoring, offering simultaneous information on particle composition, surface chemistry, and adsorbed contaminant burden. Furthermore, extending this technique to additional metals and organic pollutants could enable comprehensive contaminant profiling. The demonstrated synergy between molecular and atomic spectroscopies thus provides a pathway toward compact, multi-purpose analytical instruments capable of addressing the growing analytical demand in environmental and industrial microplastic assessment.

Conclusions

This study demonstrates a compact, integrated LIBS-Raman spectroscopic platform capable of concurrent molecular identification of polymer microplastics and quantitative detection of associated heavy-metal contaminants. Raman spectroscopy enabled clear discrimination of polystyrene, polyethylene, and polypropylene through characteristic vibrational fingerprints, while LIBS analysis provided quantitative sensitivity toward Pb and Cu, yielding limits of detection of 2.29 ppm and 1.61 ppm, respectively, within a linear concentration range below 100 ppm where self-absorption effects were minimal. These detection limits are well aligned with concentration ranges reported for metal adsorption on microplastic surfaces in contaminated aquatic environments, indicating that the proposed system is suitable for practical environmental screening applications rather than solely laboratory-scale demonstrations.

Importantly, the principal novelty of this work lies in the simultaneous and spatially correlated analysis enabled by the combined platform. Unlike conventional bulk analytical approaches such as ICP-MS or AAS coupled with FT-IR or Raman spectroscopy, which require separate measurements and sample preparation steps, the present system allows direct correlation between a specific polymer type and its associated heavy-metal burden at the single-particle level. This capability provides a unique analytical advantage for investigating contaminant transport mechanisms, and potential toxicity pathways of microplastics in environmental systems.

Future work will explore mid-level data fusion approaches, in which extracted Raman features are combined with LIBS-derived elemental intensities to enable automated classification of microplastic particles according to both polymer type and contamination level. Such developments would facilitate rapid, high-throughput analysis and further strengthen the applicability of the proposed LIBS-Raman platform for *in situ*

environmental monitoring and risk assessment of microplastic pollution.

Author contributions

Sungho Shin: project administration, investigation, methodology, resource and writing, John Park: methodology and resource, Duk-Jo Kong: project administration, review & editing, funding acquisition, and supervision.

Conflicts of interest

There are no conflicts to declare.

Data availability

The data supporting the findings of this study are available within the article and its supplementary information (SI). Supplementary information: normalized spectra and full-range calibration curves. See DOI: https://doi.org/10.1039/d5ay01789k.

Acknowledgements

This work was supported by the InnoCORE program of the Ministry of Science and ICT (GIST InnoCORE KH0860).

References

1 R. C. Thompson, Y. Olsen, R. P. Mitchell, A. Davis, S. J. Rowland, A. W. John, D. McGonigle and A. E. Russell, *Science*, 2004, **304**, 838.
2 T. S. Galloway, M. Cole and C. Lewis, *Nat. Ecol. Evol.*, 2017, **1**, 0116.
3 A. A. Koelmans, A. Bakir, G. A. Burton and C. R. Janssen, *Environ. Sci. Technol.*, 2016, **50**, 3315–3326.
4 D. Eerkes-Medrano, H. A. Leslie and B. Quinn, *Curr Opin Environ Sci Health*, 2019, **7**, 69–75.
5 L. A. Holmes, A. Turner and R. C. Thompson, *Environ. Pollut.*, 2012, **160**, 42–48.
6 C. M. Rochman, E. Hoh, T. Kurobe and S. J. Teh, *Sci. Rep.*, 2013, **3**, 3263.
7 P. Bhattacharya, S. Lin, J. P. Turner and P. C. Ke, *J. Phys. Chem. C*, 2010, **114**, 16556–16561.
8 A. Käppler, D. Fischer, S. Oberbeckmann, G. Schernewski, M. Labrenz, K.-J. Eichhorn and B. Voit, *Anal. Bioanal. Chem.*, 2016, **408**, 8377–8391.
9 J. Wang, J. Peng, Z. Tan, Y. Gao, Z. Zhan, Q. Chen and L. Cai, *Chemosphere*, 2017, **171**, 248–258.
10 D. A. Cremers and L. J. Radziemski, *Handbook of Laser-Induced Breakdown Spectroscopy*, John Wiley & Sons, 2013.
11 E. Smith and G. Dent, *Modern Raman Spectroscopy: a Practical Approach*, John Wiley & Sons, 2019.
12 A. F. Mankoula, W. Tawfik, J. E. Gagnon, B. J. Fryer, F. El-Mekawy and M. E. Shaheen, *Egypt. J. Chem.*, 2021, **64**, 1167–1177.
13 M. E. Shaheen, W. Tawfik, A. F. Mankoula, J. E. Gagnon, B. J. Fryer and F. El-Mekawy, *Environ. Sci. Pollut. Res.*, 2021, **28**, 36039–36052.
14 N. Fayek, W. Tawfik, A. KhalafAllah and M. Fikry, *J. Opt.*, 2025, 1–14.
15 K. Elsayed, W. Tawfik, A. E. Khater, T. S. Kayed and M. Fikry, *Opt. Quantum Electron.*, 2022, **54**, 96.
16 W. Tawfik, L. G. Bousiakou, R. Qindeel, W. Farooq, N. H. Alonizan and A. J. Fatani, *Optoelectron. Adv. Mater., Rapid Commun.*, 2015, **9**, 185–192.
17 W. Tawfik and S. Sawaf, 2014.
18 X. X. Han, R. S. Rodriguez, C. L. Haynes, Y. Ozaki and B. Zhao, *Nat. Rev. Methods Primers*, 2021, **1**, 87.
19 N. Fayek, W. Tawfik, A. Khalafallah, S. Hamed and W. Mousa, 2021.
20 N. Fayek, W. Tawfik, A. Khalafallah, S. Hamed, W. Mousa and M. Fikry, *Minerals*, 2023, 13.
21 W. Farooq, A. S. Al-Johani, M. Alsalhi, W. Tawfik and R. Qindeel, *J. Mol. Struct.*, 2020, **1201**, 127152.
22 C. F. Araujo, M. M. Nolasco, A. M. Ribeiro and P. J. Ribeiro-Claro, *Water Res.*, 2018, **142**, 426–440.
23 Y. Li, M. Shan, Y. Wang, J. Cong, L. Ding, J. Lin, M. Cui and N. Ma, *J. Anal. At. Spectrom.*, 2025, **40**, 1995–2005.
24 A. Nardecchia, A. de Juan, V. Motto-Ros, C. Fabre and L. Duponchel, *Spectrochim. Acta, Part B*, 2022, **198**, 106571.
25 P. Colomban, *Quantum Matter*, 2014, **3**, 361–380.
26 V. Motto-Ros, D. Syvilay, L. Bassel, E. Negre, F. Trichard, F. Pelascini, J. El Haddad, A. Harhira, S. Moncayo and J. Picard, *Spectrochim. Acta, Part B*, 2018, **140**, 54–64.
27 V. Lednev, P. Sdvizhenskii, D. Liu, I. Gorudko, S. Pershin and A. Bunkin, *Spectrochim. Acta, Part B*, 2024, **213**, 106864.
28 A. Hrdlička, J. Horská, J. Hegrová, M. Bucková, D. Prochazka, J. Buday, P. Pořízka, V. Kanický and J. Kaiser, *J. Anal. At. Spectrom.*, 2025, **40**, 2426–2437.
29 J. Guezenoc, A. Gallet-Budynek and B. Bousquet, *Spectrochim. Acta, Part B*, 2019, **160**, 105688.
30 S. J. Barton, T. E. Ward and B. M. Hennelly, *Anal. Methods*, 2018, **10**, 3759–3769.
31 A. Biancolillo, F. Marini, C. Ruckebusch and R. Vitale, *Appl. Sci.*, 2020, **10**, 6544.
32 Y. Sun, E. W. Chen, J. Thomas, Y. Liu, H. Tu and S. A. Boppart, *Opt. Lett.*, 2020, **45**, 3613–3616.
33 A. Alfonso-García, J. Paugh, M. Farid, S. Garg, J. Jester and E. Potma, *J. Raman Spectrosc.*, 2017, **48**, 803–812.
34 N. A. V. Sassarini, A. Schito, M. Gasparrini, P. Michel and S. Corrado, *Int. J. Coal Geol.*, 2023, **271**, 104237.
35 T. Vincent, K. Kawahara, V. Antonov, H. Ago and O. Kazakova, *Carbon*, 2023, **201**, 141–149.
36 S. Romano, N. X. Vinh, J. Bailey and K. Verspoor, *J. Mach. Learn. Res.*, 2016, **17**, 1–32.
37 M. Rezaei and P. Fränti, *IEEE Trans. Knowl. Data Eng.*, 2016, **28**, 2173–2186.
38 S. Moncayo, S. Manzoor, F. Navarro-Villoslada and J. Caceres, *Chemom. Intell. Lab. Syst.*, 2015, **146**, 354–364.
39 J. Zeng, Y. Guo, Y. Han, Z. Li, Z. Yang, Q. Chai, W. Wang, Y. Zhang and C. Fu, *Molecules*, 2021, **26**, 749.

40 M. Mazilu, A. C. D. Luca, A. Riches, C. S. Herrington and K. Dholakia, *Opt. Express*, 2010, **18**, 11382–11395.
41 A. P. Kotula, M. W. Meyer, F. De Vito, J. Plog, A. R. Hight Walker and K. B. Migler, *Rev. Sci. Instrum.*, 2016, **87**, 105105.
42 X. Guo, Z. Lin, Y. Wang, Z. He, M. Wang and G. Jin, *Polymers*, 2019, **11**, 1698.
43 M. Dong, J. Lu, S. Yao, Z. Zhong, J. Li, J. Li and W. Lu, *Opt. Express*, 2011, **19**, 17021–17029.
44 S. Trautner, J. Jasik, C. G. Parigger, J. D. Pedarnig, W. Spendelhofer, J. Lackner, P. Veis and J. Heitz, *Spectrochim. Acta, Part A*, 2017, **174**, 331–338.
45 Y. Ralchenko, *Mem. Soc. Astron. Ital.*, **8**, 96.
46 C. M. Bishop and N. M. Nasrabadi, *Pattern Recognition and Machine Learning*, Springer, 2006.
47 Y. Guo, W. Jin, W. Wang, Z. Guo and Y. He, *Anal. Methods*, 2022, **14**, 3898–3910.
48 T. P. Forbes, J. M. Pettibone, E. Windsor, J. M. Conny and R. A. Fletcher, *Anal. Chem.*, 2023, **95**, 12373–12382.
49 V. Palleschi, *Spectroscopy*, 2022, **37**, 60–62.
50 R. Zhang, C. Song, J. Liu, T. Zhang, H. Tang and H. Li, *Anal. Chem.*, 2025, **97**, 14246–14255.
51 Z. Khan, M. H. Ullah, B. Rahman, A. I. Talukder, M. Wahadoszamen, K. Abedin and A. Haider, *J. Spectrosc.*, 2022, **2022**, 3887038.
52 C. A. D'Angelo, M. Garcimuño, D. D. Pace and G. Bertuccelli, *J. Quant. Spectrosc. Radiat. Transfer*, 2015, **164**, 89–96.
53 A. Safi, S. H. Tavassoli, G. Cristoforetti, E. Tognoni, B. Campanella, S. Legnaioli, S. Pagnotta, F. Poggialini and V. Palleschi, *Anal. Chem.*, 2019, **91**, 8595–8601.